




Cite this: DOI: 10.1039/d5nj02206a

# Plasticized composite electrolytes with mesoporous silica nanoparticle-reinforced PVDF–HFP for solid-state lithium–metal batteries†

Xi Fu,<sup>a</sup> Qi Wei, <sup>\*,a</sup> Wenyu Zheng,<sup>a</sup> Haoyu Bai,<sup>a</sup> Xinyuan Liu,<sup>a</sup> Shuai Hao<sup>\*,b</sup> and Wei Lu<sup>\*,c</sup>

The solid-state lithium polymer battery is emerging as a preferred alternative to liquid lithium-ion batteries due to its enhanced safety and superior interfacial compatibility. This study proposes a solid polymer electrolyte (SPE) design that integrates inorganic mesoporous silica nanoparticles (MSN) and plasticizer succinonitrile (SCN) into a PVDF–HFP/LiTFSI matrix, creating abundant electrochemically stable lithium-ion transport pathways and structural void spaces. Experimental results demonstrated that the as-fabricated SPEs exhibited a wide electrochemical window of 5.6 V and an ionic conductivity of  $3.1 \times 10^{-5} \text{ S cm}^{-1}$  at room temperature. Notably, the symmetric cell employing this SPEs demonstrated stable operation exceeding 500 hours under  $0.2 \text{ mA cm}^{-2}$  current density and  $0.2 \text{ mA h cm}^{-2}$  areal capacity, while maintaining consistently low polarization levels. Further investigations reveal that the all-solid-state LFP|SPEs|PDDA–TFSI@Li battery, featuring a poly(diallyl dimethyl ammonium)-bis(trifluoromethanesulfonyl)imide (PDDA–TFSI) polycationic protective layer on the lithium metal surface, delivered an impressive initial discharge capacity of  $167.6 \text{ mA h g}^{-1}$  at  $25^\circ\text{C}$  and  $0.1\text{C}$  rate. After 200 cycles at  $0.5\text{C}$  rate, it retained a high reversible capacity of  $153.8 \text{ mA h g}^{-1}$  with exceptional capacity retention rate (97.2%).

Received 26th May 2025,  
Accepted 23rd July 2025

DOI: 10.1039/d5nj02206a

rsc.li/njc

## Introduction

In the context of the rapid development of portable electronic devices, electric vehicles, and large-scale energy storage systems, the development of advanced energy storage technologies that combine high energy density, high safety, and low cost has become a core challenge in the global energy sector.<sup>1–4</sup> Due to the incomparable advantage of lithium-ion batteries (LIBs) in energy density compared to other types of rechargeable batteries, LIBs undoubtedly dominate the electrochemical energy storage market.<sup>5–7</sup> However, traditional LIBs are limited by the flammability of liquid organic electrolytes and the dendrite growth issue of lithium metal anodes, making it difficult for achieving high energy density and safety to meet the requirements of next-generation applications.<sup>8–10</sup> Solid-state lithium metal batteries (SSLMBs), which combine lithium metal anodes with high

theoretical specific capacity and solid-state electrolytes with high safety, demonstrate breakthrough potential. However, the brittleness of inorganic solid-state electrolytes (such as sulfides/oxides) and the low ionic conductivity of organic solid-state electrolytes hinder their practical application.<sup>11–14</sup>

SPEs have become a research hotspot due to their unique processability, interfacial compatibility, and cost advantages.<sup>15–18</sup> As a typical matrix material for SPEs, poly(vinylidene fluoride-co-hexafluoropropylene) (PVDF–HFP) demonstrates promising potential owing to its robust mechanical strength, outstanding tolerance to high voltages, and high dielectric constant.<sup>19–23</sup> Unfortunately, its high crystallinity leads to low ambient-temperature ionic conductivity and flammability issues, which can easily cause lithium dendrite growth and lithium metal battery failure.<sup>24–26</sup> In view of the above, it is crucial to construct PVDF–HFP-based SPEs that combine excellent mechanical properties, outstanding ionic conductivity, and safety.<sup>27–29</sup> To date, researchers have proposed various modification strategies to enhance the comprehensive performance of SPEs. A feasible solution is the addition of plasticizers. The most commonly used plasticizers are ethylene carbonate (EC),<sup>30</sup> SCN,<sup>31</sup> and fluoroethylene carbonate (FEC).<sup>32</sup> Although these plasticizers significantly enhance the ionic conductivity of SPEs, their flammability and volatility may raise safety concerns.<sup>33</sup> Incorporating inorganic

<sup>a</sup> Chengdu University of Technology, Chengdu, Sichuan 610059, P. R. China.  
E-mail: weiqi2023@cdut.edu.cn

<sup>b</sup> China FAW Group Co., LTD, State Key Laboratory of Advanced Vehicle Integration and Control Changchun, 130013, P. R. China

<sup>c</sup> Institute of Advanced Materials, Nanjing University of Posts and Telecommunications, Nanjing, Jiangsu 210023, P. R. China

† Electronic supplementary information (ESI) available. See DOI: <https://doi.org/10.1039/d5nj02206a>

fillers into SPEs is an effective strategy to improve their safety, electrochemical performance, and mechanical strength.<sup>34,35</sup> The most frequently employed inorganic fillers are silica ( $\text{SiO}_2$ ),<sup>36,37</sup> titania ( $\text{TiO}_2$ ),<sup>38</sup> and alumina ( $\text{Al}_2\text{O}_3$ ),<sup>39</sup> which can improve ionic conduction by reducing the crystallinity of SPEs or providing interfacial transport pathways. However, an excessively high filler content in SPEs may reduce the energy density of the battery.<sup>40</sup> Li *et al.* found that silica forms a large contact area with the polymer electrolyte, and the interface between the polymer electrolyte and the filler provides abundant ion transport channels.<sup>41</sup> Hu *et al.* incorporated lithium sulfonated poly(vinyl alcohol) and silica particles into a poly(ethylene oxide) (PEO)-based SPE, forming a three-dimensionally crosslinked inorganic/organic composite SPE. The synergistic addition of lithium sulfonated poly(vinyl alcohol) and silica reduced polymer crystallinity, thereby promoting the segmental motion of PEO and enhancing the dissociation of the LiTFSI salt. The Lewis acid sites of  $\text{SiO}_2$  can effectively immobilize the TFSI<sup>−</sup> anion, thereby releasing a higher concentration of free  $\text{Li}^+$  ions.  $\text{SiO}_2$  also exhibits promising flame retardancy, ensuring the safety of the SPE material.<sup>42</sup> Fang *et al.* found that the introduction of a  $\text{SiO}_2$  aerogel endows the polymer electrolyte with excellent thermal stability and flame retardancy. Meanwhile, the interaction between the hydroxyl groups on the surface of  $\text{SiO}_2$  particles and PVDF-HFP forms a strong cross-linked structure, enhancing the mechanical strength and stability of the electrolyte. Additionally, the presence of the  $\text{SiO}_2$  aerogel and  $\text{Li}_{6.4}\text{La}_3\text{Zr}_{1.4}\text{Ta}_{0.6}\text{O}_{12}$  (LLZTO) promotes the dissociation of lithium salts through Lewis acid–base interactions, enabling the electrolyte to exhibit enhanced electrochemical performance.<sup>43</sup> Didwal *et al.* employed highly mesoporous silica nanoparticles as fillers for polycarbonate to prepare cost-effective and highly stable SPEs. The researchers attributed the enhanced electrochemical performance of the SPEs to the large specific surface area of silica, which interacts closely with the polymer matrix and provides a low-tortuosity polymer–ceramic phase for rapid lithium-ion transport.<sup>44</sup> Interfacial thermal conduction of SPEs, an easily overlooked structural property, has been demonstrated to significantly affect the structural stability and compatibility of the electrode–electrolyte interface under high-temperature and/or fast-charging conditions.<sup>45–48</sup> Li *et al.* thoroughly investigated the enhancement effect of densified polyacrylonitrile/silica nanofiber membranes on the structural performance of polymer electrolytes. The results demonstrate that, in addition to excellent mechanical properties, the SPEs also exhibit good high-temperature structural stability due to its efficient thermal conduction effect.<sup>49</sup> However, single-functional additives cannot simultaneously enhance the safety, ionic conductivity, and interfacial stability of SPEs. Therefore, dual fillers are urgently needed to balance and enhance the comprehensive performance of SPEs.

Consequently, we have meticulously designed a dual-filler-enhanced PVDF-HFP-based SPE. By incorporating MSN inorganic ceramic fillers and SCN plasticizer into PVDF-HFP, we endow lithium metal batteries (LMBs) with excellent electrochemical performance and safety. MSN offers advantages such as low cost, high mesoporosity, high stability, the ability to reduce polymer crystallinity and surface Lewis acidity, and the

promotion of lithium salt dissociation. SCN can modify the morphology of SPEs, forming a three-dimensional interpenetrating network, effectively reducing crystallinity and expanding the amorphous regions. Benefiting from the synergistic effect of SCN and MSN, the meticulously designed SPE exhibits excellent ionic conductivity, electrochemical window, activation energy, thermal stability, and flame retardancy. Testing of symmetric lithium metal batteries reveals that the SPEs can operate stably for over 500 hours at a current density of  $0.2 \text{ mA cm}^{-2}$  and an areal capacity of  $0.2 \text{ mA h cm}^{-2}$ , while maintaining a consistently low polarization level. Furthermore, to avoid side reactions between SCN and lithium metal, a polycationic protective layer is constructed on the lithium metal surface. The LFP|SPEs|PDDA-TFSI@Li all-solid-state lithium metal battery demonstrates a discharge capacity of  $153.8 \text{ mA h g}^{-1}$ , a capacity retention rate of 97.2%, and a coulombic efficiency close to 100% after 200 cycles at a rate of 0.5C.

## Experimental

### Preparation of materials

0.32 g of cetyltrimethylammonium bromide (CTAB) and 1 mL of ammonia solution were added to a mixed solution of 150 mL of deionized water and 60 mL of ethanol, and the mixture was stirred continuously at  $35^\circ\text{C}$  for 1 hour. Then, 1 mL of tetraethyl orthosilicate (TEOS) was added to the above mixture, and the mixture was stirred continuously at  $35^\circ\text{C}$  for 3 hours. After the reaction solution was cooled to room temperature, the precipitate was collected by centrifugation and washed multiple times with ethanol and water by centrifugation to obtain a white precipitate. The white precipitate was dispersed in a mixed solution of 200 mL of ethanol and 0.4 mL of hydrochloric acid and stirred continuously at  $60^\circ\text{C}$  for 3 hours. After the reaction solution was cooled to room temperature, the precipitate was collected by centrifugation, and this step was repeated 3 times. The precipitate was collected by centrifugation and washed multiple times with ethanol and water by centrifugation to obtain a white precipitate. The white precipitate was vacuum-dried to obtain the MSN product, which was used for the synthesis of composite solid polymer electrolytes.<sup>50</sup>

PVDF-HFP, SCN, and LiTFSI were dissolved in *N*-methyl-2-pyrrolidone (NMP) at a mass ratio of 8:4:2 and stirred continuously for 10 hours at  $30^\circ\text{C}$ . Different mass percentages of MSN (relative to the total mass of PVDF-HFP, SCN, MSN, and LiTFSI) were added to the aforementioned solution, followed by continuous ultrasonic treatment for 3 hours. The composite polymer electrolyte films prepared by adding  $x \text{ wt}\%$  ( $x = 1, 2, 3$ , and 4) MSN were designated as PSM $x$ . The mixed solution was cast onto a clean glass plate and vacuum-dried at  $60^\circ\text{C}$  for 24 hours, yielding uniform SPE membranes. The resultant composite polymer electrolyte membranes were punched into 19 mm diameter circular discs for subsequent battery assembly applications.

The components were weighed according to a mass ratio of  $\text{LiFePO}_4$  (LFP):conductive agent (acetylene black):binder

(PVDF):plasticizer (SCN) = 7 : 1:1 : 1. PVDF and SCN were added to NMP and stirred continuously at 60 °C for 12 hours. The two powders of acetylene black and LFP were uniformly mixed in an agate mortar. After the mixture was cooled to room temperature, the mixture was added to the mortar, and grinding was continued to obtain a viscous slurry. The slurry was coated on the surface of the aluminum foil and vacuum-dried at 60 °C for 12 hours to completely remove the solvent. The dried LFP electrode was cut into round discs with a diameter of 12 mm for subsequent battery assembly.

PDDA-TFSI@Li was prepared according to the previously reported methods.<sup>51</sup>

### Materials characterization

The spectral data of SPEs in the wavenumber range of 400–4000 cm<sup>−1</sup> were collected using a Thermo Fisher Scientific Nicolet iS20 Fourier transform infrared (FTIR) spectrometer. The effects of SCN and MSN on the crystallization behavior of PVDF-HFP were analyzed using a Bruker D8 Advance X-ray diffractometer (XRD). The thermal properties of the materials were evaluated using a NETZSCH STA409PC thermogravimetric analyzer (TGA) at a heating rate of 10 °C min<sup>−1</sup> under a nitrogen atmosphere. The high-resolution morphology of MSN, the effects of SCN and MSN on the surface morphology of PVDF-HFP, and the morphology and distribution state of the LFP electrode were observed using a high-resolution transmission electron microscope (HR-TEM, FEI Talos 200x), a scanning electron microscope (SEM, ZEISS Sigma 360), and energy-dispersive X-ray spectroscopy (EDS). The mechanical properties of SPEs were tested using an HS-3004B-S electronic universal testing machine.

### Electrochemical test

Electrochemical impedance spectroscopy (EIS) analysis was performed on stainless steel (SS)|SPEs|SS symmetric cells using an electrochemical workstation (Shanghai Chenhua CHI760E) at room temperature (25 °C) in the frequency range of 10<sup>6</sup> Hz to 10<sup>2</sup> Hz. EIS analysis was also conducted on SPEs in the temperature range of 30 °C to 80 °C. The ionic conductivity ( $\sigma$ ) was calculated using eqn (1):

$$\sigma = \frac{L}{R_b \times A} \quad (1)$$

In the equation,  $R_b$  is the measured impedance,  $L$  and  $A$  represent the thickness of the electrolyte and the contact area between the electrode and the electrolyte, respectively.

The ion transport activation energy ( $E_a$ ) of SPEs was calculated using eqn (2):

$$\sigma = A \exp\left(-\frac{E_a}{RT}\right) \quad (2)$$

In the equation,  $\sigma$  is the ionic conductivity,  $A$  is the pre-exponential factor,  $E_a$  is the pseudo-activation energy,  $R$  is the molar gas constant, and  $T$  is the thermodynamic temperature. By plotting the relationship curve between  $\log_{10} \sigma$  and  $1000/T$ , the  $E_a$  value can be obtained from the slope.

To evaluate the electrochemical stability window of the SPEs, a Li|SPEs|SS cell was assembled, with the stainless steel

plate connected to the working electrode and ground wire, and the lithium anode connected to the counter electrode and reference electrode, and scanned in the voltage range of 0–6 V at a scan rate of 0.1 mV s<sup>−1</sup>. At room temperature, chronoamperometry (CA) was used to perform a DC polarization experiment on the SS|SPEs|SS cell by gradually increasing the voltage from 0.1 V to 0.5 V. The assembled LFP|SPEs|PDDA-TFSI@Li batteries were subjected to rate performance and cycling performance tests using a Landt battery testing system (Wuhan Landt CT3001A) at 25 °C. Galvanostatic charge–discharge tests were performed on PDDA-TFSI@Li|SPEs|PDDA-TFSI@Li batteries.

## Results and discussion

The increased fraction of amorphous regions in SPEs facilitates the motion of flexible chain segments, thereby driving Li<sup>+</sup> migration through the 3D polymer network and establishing continuous, rapid Li<sup>+</sup> transport channels.<sup>52–54</sup> Therefore, the addition of plasticizers and doping with inorganic fillers can disrupt the crystalline domains of the polymer and increase the proportion of amorphous regions.<sup>55–57</sup> Fig. 1a illustrates the roles of SCN and MSN, two functional fillers, in lithium metal batteries (LMBs). PVDF-HFP has a low proportion of amorphous regions (high crystallinity), resulting in low ionic conductivity.<sup>24–26</sup> Previous work has confirmed that SCN can construct rapid Li<sup>+</sup> transport channels by changing the morphology of PVDF.<sup>58</sup> In this study, PVDF-HFP/SCN was first prepared by incorporating SCN into the PVDF-HFP polymer matrix, forming conductive pathways that enhance ionic conductivity and facilitate efficient lithium-ion (Li<sup>+</sup>) transport. The hydrogen bonding interactions between inorganic filler SiO<sub>2</sub> nanoparticles and polymer chains increased interchain friction, while the cross-linked network structure further inhibited the reorganization of polymer chains, leading to a decrease in polymer crystallinity.<sup>59,60</sup> SiO<sub>2</sub>, as a strongly acidic oxide with abundant Lewis acid sites, exhibits strong affinity for

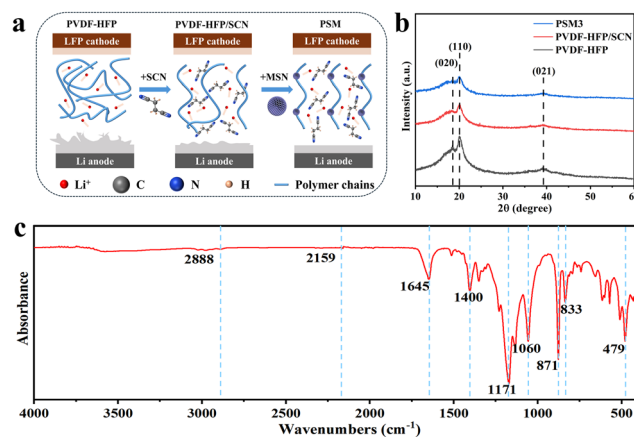


Fig. 1 (a) Schematic illustration of the SPE design architecture. (b) XRD patterns of PVDF-HFP, PVDF-HFP/SCN, and PSM3. (c) FTIR spectrum of PSM3.

electronegative species. The introduction of SiO<sub>2</sub> into the system can enhance the interaction between the filler and anions, forming an interconnected network that promotes Li<sup>+</sup> conduction. In SiO<sub>2</sub>-filled SPEs, Li<sup>+</sup> migrates through a hopping mechanism between negatively charged sites on filler-anion pairs.<sup>37</sup> To further improve the performance, MSN was added to PVDF-HFP/SCN to prepare PVDF-HFP/SCN/MSN. MSN improves ionic conduction by reducing the crystallinity of PVDF-HFP and providing lithium-ion transport channels. The synergistic effect of SCN and MSN endows SPEs with structural stability and compatibility at the electrode-electrolyte interface under rapid charge-discharge conditions, as well as excellent thermal stability and flame-retardant properties. This dual modification makes SPEs promising electrolytes for high-stability and high-safety energy storage systems.

Fig. 1b shows the XRD patterns of PVDF-HFP, PVDF-HFP/SCN, and PSM3. The XRD pattern of PVDF-HFP showed the characteristic peaks at 18.24°, 20.10°, and 39.08°, corresponding to the (020), (110), and (021) crystal planes, respectively. The diffraction peak intensities of PVDF-HFP at 18.24°, 20.10°, and 39.08° decrease, which is attributed to the introduction of SCN and MSN. This indicates that the addition of SCN and MSN can reduce the crystallinity of PVDF-HFP, and the proportion of amorphous regions in PVDF-HFP increases significantly. The decrease in crystallinity is beneficial for enhancing the lithium-ion transport capability of the composite electrolyte at room temperature. Quantitative analysis of the proportion between free TFSI<sup>-</sup> anions and Li<sup>+</sup>-TFSI<sup>-</sup> ion pairs in different SPEs was performed *via* FTIR, where the pink and green peak areas correspond to the proportions of free-state TFSI<sup>-</sup> and Li<sup>+</sup>-TFSI<sup>-</sup> ion pairs, respectively (Fig. S3, ESI†). After spectral fitting analysis, when the SCN filler was added to PVDF-HFP, the characteristic peak intensity at 740 cm<sup>-1</sup> (dissociated ions) increased by 20.78%. Following the subsequent addition of MSN filler, the peak at 745 cm<sup>-1</sup> (undissociated ion pairs) decreased by 25.23%.<sup>61</sup> Fig. 1c illustrates the FTIR spectrum of PSM3. FTIR analysis was employed to identify the functional groups present in PSM3 and confirm the existence of SCN and MSN. The FTIR data reveals that the characteristic peak at 1400 cm<sup>-1</sup> corresponds to the angular deformation vibration of -CH<sub>2</sub>-, associated with the crystalline phase of PVDF-HFP. Peaks at 1171 cm<sup>-1</sup> and 1060 cm<sup>-1</sup> arise from the stretching vibrations of -CF<sub>2</sub>- groups,<sup>62</sup> while the features at 833 cm<sup>-1</sup> and 871 cm<sup>-1</sup> are attributed to the amorphous phase of PVDF-HFP. Several peaks related to SCN appear at 2888 cm<sup>-1</sup>, and the peak at 2159 cm<sup>-1</sup> corresponds to the C≡N stretching vibrations of SCN,<sup>63</sup> confirming that SCN exists in a free state within the solid electrolyte without reacting with other organic components. The characteristic peak at 479 cm<sup>-1</sup> corresponds to the bending vibration of Si-O bonds in MSN.

SEM images of PVDF-HFP, PVDF-HFP/SCN, MSN, and PSM3, along with HR-TEM images of MSN, are presented in Fig. 2(a), (b), (c), (e) and (f), and (d), respectively. SEM analysis reveals that PVDF-HFP exhibits high crystallinity, characterized by spherical structures with large and uneven diameters

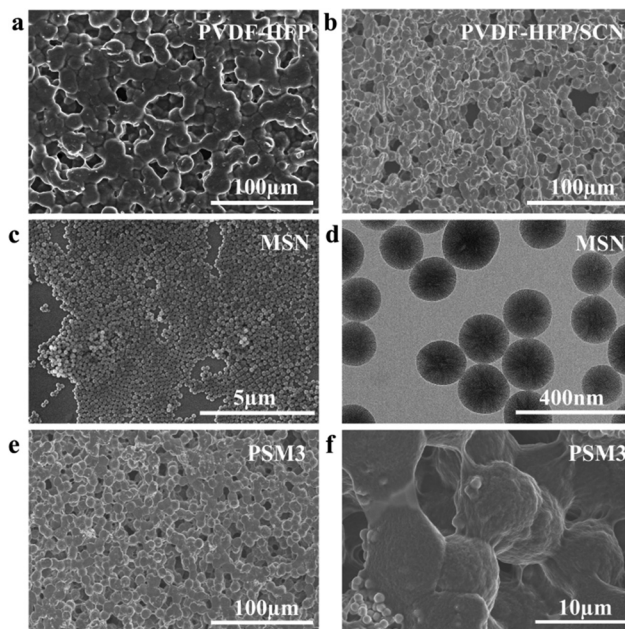
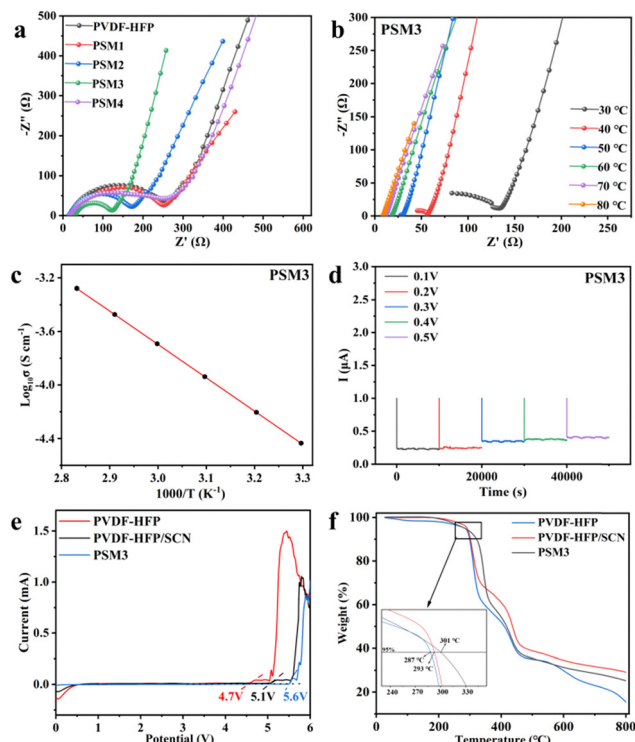


Fig. 2 SEM images of (a) PVDF-HFP, (b) PVDF-HFP/SCN, (c) MSN, and (e) and (f) PSM3. (d) HR-TEM image of MSN.

(approximately 9–16 μm), exhibiting aggregation and low porosity (Fig. 2a). In contrast, PVDF-HFP/SCN demonstrates regular spherical structures with uniform size (approximately 9 μm) and significantly enhanced porosity, forming a porous interconnected network without surface aggregation. These observations confirm the excellent dispersion of SCN in PVDF-HFP, effectively reducing crystallinity (Fig. 2b). Fig. 2c and Fig. S4 (ESI†) illustrate the uniform size and homogeneous dispersion of MSN particles. HR-TEM data reveal that MSN possesses abundant mesoporous structures with diameters around 200 nm (Fig. 2d). SEM images of PSM3 confirm the uniform dispersion of MSN within the matrix (Fig. 2e and Fig. S5, ESI†). Fig. 2f exhibits interconnected spherical structures (approximately 8 μm in diameter) forming a network, indicating that MSN incorporation further reduces the PVDF-HFP crystallinity and successfully constructs a 3D ion transport pathway, facilitating lithium-ion conduction.

EIS measurements were conducted using SS|SPEs|SS symmetric cells to analyze the effects of MSN filler content and temperature on the ionic conductivity of the PVDF-HFP matrix. The EIS of PVDF-HFP-based solid polymer electrolytes with varying MSN contents are presented in Fig. 3a and Table S2 (ESI†). At 25 °C, the ionic conductivities of PVDF-HFP, PSM1, PSM2, PSM3, and PSM4 were measured to be  $1.52 \times 10^{-5}$ ,  $2.06 \times 10^{-5}$ ,  $2.26 \times 10^{-5}$ ,  $3.10 \times 10^{-5}$ , and  $1.68 \times 10^{-5}$  S cm<sup>-1</sup>, respectively. These results indicate a significant increase in ionic conductivity with increasing MSN content, followed by a slight decrease when MSN content becomes excessive. This trend is attributed to the percolation threshold being exceeded, leading to increased impedance at the ceramic-polymer interface and restricting lithium-ion transport primarily to ceramic-polymer pathways.<sup>44</sup> The results demonstrate that the electrolyte



**Fig. 3** (a) EIS plots of PVDF-HFP-based solid electrolytes with varying MSN filler contents measured at 25 °C. (b) EIS spectra of SS|PSM3|SS symmetric cells across the 30–80 °C range. (c) Arrhenius plot of PSM3. (d) DC polarization curves of PSM3 under different voltage conditions. (e) LSV curves of PVDF-HFP, PVDF-HFP/SCN, and PSM3 at 25 °C. (f) TGA curves of PVDF-HFP, PVDF-HFP/SCN, and PSM3.

membrane achieves maximum ionic conductivity ( $3.1 \times 10^{-5} \text{ S cm}^{-1}$ ) when the MSN content reaches 3 wt%. Fig. 3b illustrates the temperature-dependent ionic conductivity of PSM3 electrolytes: ionic conductivity progressively increases with increasing temperature, reaching  $4.5 \times 10^{-4} \text{ S cm}^{-1}$  at 80 °C. Based on the Arrhenius equation, the calculated activation energy for PSM3 electrolytes is 0.49 eV, indicating lower energy barriers for lithium-ion migration within this electrolyte system (Fig. 3c and Fig. S11, ESI<sup>†</sup>). While high ionic conductivity is desirable, low electronic conductivity is equally critical for suppressing dendrite growth at the lithium metal anode–solid electrolyte interface.<sup>64,65</sup> Direct current polarization measurements on SS|PSM3|SS symmetric cells confirm its sufficiently low electronic conductivity ( $8.4 \times 10^{-7} \text{ S cm}^{-1}$ , as shown in Fig. 3d and Table S4, ESI<sup>†</sup>). The electronic conductivities of PVDF-HFP and PVDF/SCN were relatively high, reaching  $1.11 \times 10^{-6} \text{ S cm}^{-1}$  and  $9.01 \times 10^{-7} \text{ S cm}^{-1}$ , respectively (Fig. S13 and Table S5, S6, ESI<sup>†</sup>). The electrochemical stability of the SPEs was evaluated using linear sweep voltammetry (LSV) as shown in Fig. 3e. The LSV curves show that PSM3 has a wide electrochemical window of 5.6 V, significantly higher than the 4.7 V and 5.1 V of PVDF-HFP and PVDF/SCN, respectively. This enhanced electrochemical window indicates a substantial improvement in PSM3 stability, enabling operation across a wider potential range and supporting the development of high-voltage lithium metal

batteries. The thermal stability of SPEs under high-temperature conditions ensures the safety of PVDF-HFP-based solid-state lithium metal batteries.<sup>66,67</sup> TGA was utilized to evaluate the thermal stability of PSM3 (Fig. 3f and Fig. S14, ESI<sup>†</sup>). The onset temperature of thermal degradation is typically defined as the temperature at which 95% weight loss occurs. TGA data reveal that PSM3 begins to decompose at 301 °C (95% weight loss), which is significantly higher than the decomposition temperatures of PVDF-HFP (287 °C) and PVDF-HFP/SCN (293 °C). The incorporation of dual fillers (MSN and SCN) increases the thermal decomposition temperature of PSM3 by 14 °C, demonstrating that PSM3 exhibits sufficient thermal stability to meet the requirements for practical applications. Fig. S10 (ESI<sup>†</sup>) compares the structural stability of PVDF-HFP and PSM3 under high-temperature conditions. PVDF-HFP undergoes shrinkage and deformation after 48 hours of exposure at 180 °C, whereas PSM3 exhibits no significant changes. The exceptional mechanical strength of SPEs is critical for suppressing lithium dendrite growth.<sup>68–70</sup> As depicted in Fig. S16 (ESI<sup>†</sup>), PSM3 demonstrates a tensile strength of 2.91 MPa and an elongation at break of 5.13%. Flame retardancy test results demonstrate that PVDF-HFP begins to char within 5 seconds of direct flame exposure and becomes completely charred within 20 seconds. In contrast, while PSM3 also starts to char after 5 seconds of flame exposure, the charred area remains relatively stable after 7 seconds with minimal progression (Fig. S15, ESI<sup>†</sup>). This observation confirms that the incorporation of dual fillers (MSN and SCN) imparts a significant degree of flame retardancy to the PSM3 composite.

Despite achieving high ionic conductivity in electrolyte membranes through dual-filler incorporation, their direct implementation in lithium metal batteries remains problematic. This challenge arises from the tendency of SCN to undergo *in situ* polymerization on the lithium metal surface, which gradually depletes active SCN species and increases internal resistance during repeated charge/discharge cycles. To address this issue, surface modification of lithium metal is essential prior to assembling all-solid-state batteries, creating a protective interlayer that suppresses undesirable electrode–electrolyte side reactions. As demonstrated in previous studies, PDDA-TFSI represents a promising polycationic protective layer characterized by its dense structure, efficient lithium-ion transport capability, and effective suppression of lithium dendrite formation. When applied in lithium metal solid-state batteries, this protective layer significantly mitigates parasitic reactions at the interface.<sup>69</sup> Inspired by this approach, we fabricated PDDA-TFSI@Li|PSM3|PDDA-TFSI@Li symmetric cells and conducted electrochemical performance tests to investigate the impact of PSM3 on lithium plating/stripping behavior. As illustrated in Fig. 4a, the interfacial stability of these symmetric cells was evaluated at current densities spanning 0.05 to 0.2 mA cm<sup>-2</sup>. The results demonstrate stable lithium insertion/extraction overpotentials over 120 hours despite fluctuations in the current density. The lithium insertion/extraction overpotential shows a gradual decrease between 120 and 130 hours, eventually stabilizing at 50 mV. Fig. 4b presents the lithium insertion/extraction overpotentials at 0.2 mA cm<sup>-2</sup> and

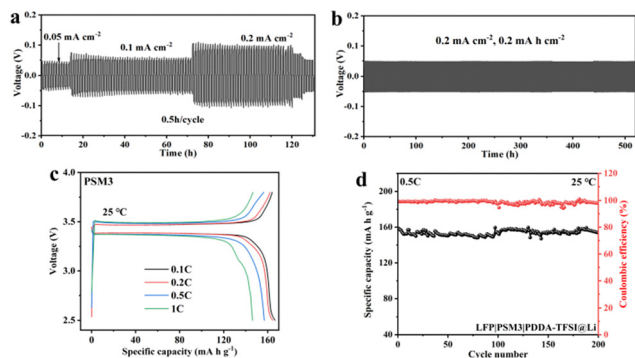


**Fig. 4** (a) Cyclic charge/discharge profiles of PDDA-TFSI@Li|PSM3|PDDA-TFSI@Li symmetric cells at the current densities of 0.05, 0.1, and 0.2 mA cm<sup>-2</sup>. (b) Long-term cycling performance of the symmetric cell at 0.2 mA cm<sup>-2</sup> with a fixed areal capacity of 0.2 mA h cm<sup>-2</sup>. (c) Rate capability characterization of LFP|PSM3|PDDA-TFSI@Li full cells showing charge/discharge profiles at various C-rates (0.1C to 1C). (d) Cycling stability of the full cell at 0.5C rate.

0.2 mA h cm<sup>-2</sup>, revealing that the PSM3-based symmetric cell maintains stable operation with minimal polarization (50 mV) exceeding 500 hours. This confirms the exceptional long-term stability achieved through the synergistic combination of PSM3 and the PDDA-TFSI@Li interface. SEM characterization of the lithium metal surface revealed the morphology of the PDDA-TFSI protective layer, while EDS mapping confirmed its composition (Fig. S8, S9, ESI<sup>†</sup>). SEM images (Fig. S8, ESI<sup>†</sup>) demonstrate successful formation of a dense polycationic protective layer on the lithium anode. Elemental mapping (Fig. S9, ESI<sup>†</sup>) confirms the homogeneous distribution of C, N, F, and S elements throughout the PDDA-TFSI film structure. Additionally, Fig. S12 (ESI<sup>†</sup>) highlights the remarkable ambient stability of PDDA-TFSI@Li compared to bare lithium metal.

In light of the wide electrochemical window and exceptional interfacial stability exhibited by PSM3, we constructed all-solid-state batteries using an LFP cathode and a PDDA-TFSI@Li anode to evaluate the electrochemical performance of PSM3 as the electrolyte matrix. The initial charge/discharge profiles of LFP|SPES|PDDA-TFSI@Li cells fabricated with varying MSN filler contents, tested at a 0.1C rate (Fig. S17 and Table S1, ESI<sup>†</sup>), demonstrate a gradual enhancement in specific capacity as the MSN content increases up to 3 wt%. However, this capacity improvement trend reverses when the MSN filler content reaches 4 wt%, resulting in a noticeable capacity decline. This observation aligns with our previous findings regarding the optimal filler content for balancing ionic conductivity and interfacial resistance in these composite electrolytes. These findings indicate that 3 wt% MSN content represents the optimal filler ratio for maximizing the specific capacity of PVDF-HFP-based electrolytes. The rate capability of the LFP|PSM3|PDDA-TFSI@Li cell is demonstrated in Fig. 4c, showing initial charge/discharge profiles at various C-rates. The cell delivers stable specific capacities of 167.6, 166.0, 151.1, and 146.5 mA h g<sup>-1</sup> at 0.1C, 0.2C, 0.5C, and 1C rates respectively. Notably, the cell achieves a maximum discharge capacity of 159.6 mA h g<sup>-1</sup> at 0.5C rate while maintaining excellent

capacity retention (97.2% after 200 cycles). Furthermore, the all-solid-state battery exhibits remarkably stable coulombic efficiency approaching 100% throughout the entire 200-cycle test duration, as shown in Fig. 4d and Fig. S18 (ESI<sup>†</sup>).

## Conclusions

This study successfully developed a dual-filler reinforcement strategy, synergistically integrating MSN and SCN into the PVDF-HFP matrix. This integration aims to enhance the electrochemical performance and flame retardancy of the SPEs. Furthermore, a polycationic protective layer was fabricated on the lithium metal surface, leading to the development of high-performance and highly safe all-solid-state lithium metal batteries. Notably, both SCN and MSN contribute to reducing the crystallinity of PVDF-HFP. FTIR spectroscopy confirmed that the dual-filler doping synergistically promotes the dissociation process of LiTFSI, resulting in an increased proportion of free TFSI<sup>-</sup> ions. Particularly, MSN additionally enhances the flame retardancy of SPEs. Therefore, the prepared dual-filler reinforced PSM3 exhibits higher ionic conductivity ( $3.10 \times 10^{-5}$  S cm<sup>-1</sup>) and lower activation energy (0.49 eV) at 25 °C compared to the pristine PVDF-HFP matrix ( $1.52 \times 10^{-5}$  S cm<sup>-1</sup> and 0.53 eV, respectively). Benefiting from these unique electrochemical properties, the fabricated LFP|PSM3|PDDA-TFSI@Li battery demonstrates remarkable lithium dendrite suppression capability, maintaining stable cycling for 200 cycles at a 0.5C rate with nearly 100% coulombic efficiency. This design concept of dual-filler reinforced polymer electrolytes offers a novel perspective for the development of advanced solid-state lithium metal batteries.

## Author contributions

Xi Fu and Qi Wei designed the study, conducted the experiments, wrote the initial draft of the manuscript, and made great contributions to the revision. Qi Wei provided project funding support for this work. Wenyu Zheng, Haoyu Bai and Xinyuan Liu synthesized the mesoporous silica. Shuai Hao and Wei Lu designed and wrote part of the initial draft. All authors reviewed and approved the final manuscript.

## Conflicts of interest

There are no conflicts to declare.

## Data availability

The data that support the findings of this study are available in the ESI<sup>†</sup> of this article.

## Acknowledgements

We sincerely acknowledge the financial support from the Chengdu University of Technology Research Start-up Fund

(10912-KYQD2023-09877) and the Chengdu University of Technology Higher Education Talent Cultivation Quality and Teaching Reform Project (JG2430071).

## Notes and references

- H. C. Wang, J. Song, K. Zhang, Q. Fang, Y. X. Zuo, T. H. Yang, Y. L. Yang, C. Gao, X. F. Wang, Q. Q. Pang and D. G. Xia, *Energy Environ. Sci.*, 2022, **15**, 5149–5158.
- Y. M. Jin, R. F. Lin, Y. M. Li, X. B. Zhang, S. P. Tan, Y. Shuai and Y. P. Xiong, *Angew. Chem., Int. Ed.*, 2024, **63**, e202403661.
- X. T. Deng, J. Chen, X. Jia, X. Y. Da, Y. J. Zhao, Y. Y. Gao, Y. Gao, X. P. Kong, S. J. Ding and G. X. Gao, *Angew. Chem., Int. Ed.*, 2024, **63**, e202410818.
- D. Y. Yu, J. K. Min, F. Lin and L. A. Madsen, *Adv. Mater.*, 2024, **36**, 2312513.
- S. J. Wang, Q. Lv, Y. T. Jing, B. Wang, D. L. Wang, H. K. Liu and S. X. Dou, *Energy Storage Mater.*, 2024, **69**, 103390.
- H. C. Wang, Y. L. Yang, C. Gao, T. Chen, J. Song, Y. X. Zuo, Q. Fang, T. H. Yang, W. K. Xiao, K. Zhang, X. F. Wang and D. G. Xia, *Nat. Commun.*, 2024, **15**, 2500.
- J. Lu, B. F. Sheng, M. F. Chen, M. Xu, Y. Y. Zhang, S. Zhao, Q. Q. Zhou, C. Y. Li, B. Wang, J. J. Liu, J. Z. Chen, Z. C. Lou and X. Han, *Energy Storage Mater.*, 2024, **71**, 103570.
- Y. Chai, D. Ning, D. Zhou, J. S. Gao, J. L. Ni, G. Y. Zhang, R. Gao, W. Wu, J. Wang and Y. L. Li., *Nano Energy*, 2024, **130**, 110160.
- X. Wang, L. S. Xu, M. S. Li, Y. Y. Hu, N. Wang, Y. Z. Meng, K. Yang and K. R. Deng, *Energy Storage Mater.*, 2024, **73**, 103778.
- F. Pei, Y. M. Huang, L. Wu, S. Y. Zhou, Q. Kang, W. J. Lin, Y. Q. Liao, Y. Zhang, K. Huang, Y. Shen, L. X. Yuan, S. G. Sun, Z. Li and Y. H. Huang, *Adv. Mater.*, 2024, **36**, 2409269.
- H. X. Liu, L. Q. Xu, F. J. Zhu, D. Z. Luo, Y. Zhang, W. T. Deng, G. Q. Zou, H. S. Hou and X. B. Ji, *Nano Energy*, 2024, **126**, 109623.
- J. P. Zhang, J. Zhu, R. Q. Zhao, J. Liu, X. C. Song, N. Xu, Y. S. Liu, H. T. Zhang, X. J. Wan and Y. F. Ma, *Energy Environ. Sci.*, 2024, **17**, 7119–7128.
- K. X. Mu, W. L. Dong, W. J. Xu, Z. N. Song, R. X. Wang, L. Y. H. Wu, H. Li, Q. Liu, C. Z. Zhu, J. Xu and L. Tian, *Adv. Funct. Mater.*, 2024, **34**, 2405969.
- R. H. Wang, W. Y. Wang, Y. Z. Zhang, W. Hu, L. Yue, J. H. Ni, W. Q. Zhang, G. Pei, S. F. Yang and L. F. Chen, *Angew. Chem., Int. Ed.*, 2025, **64**, e202417605.
- X. Han, J. J. Lu, Q. Y. Zou, H. L. Wang, M. F. Chen, T. F. Liu, R. Z. Liu, X. F. Wang, S. Y. Zhao, M. M. Zhao, B. F. Sheng, Y. Z. Chen, J. Z. Chen, R. Wen, Z. Q. Tian, Z. Q. Peng and G. M. Zhong, *Adv. Mater.*, 2025, **37**, 2504419.
- Y. Song, H. T. Qu, Z. J. Lao, X. Xiao, G. X. Lu, Y. Z. Song, L. Nie, J. Wang, J. L. Yang, Y. F. Zhu and G. M. Zhou, *Adv. Mater.*, 2025, **37**, 2419271.
- C. P. Li, Y. Zhong, R. F. Liao, T. Yi, M. H. Zhou, R. L. Liu, S. H. Liu and D. C. Wu, *Adv. Mater.*, 2025, **37**, 2500142.
- X. X. Zhao, C. Wang, X. M. Fan, Y. Li, D. B. Li, Y. L. Zhang and L. Z. Fan, *InfoMat*, 2025, **7**, e70012.
- S. F. Wen, Z. F. Sun, X. Y. Wu, S. H. Zhou, Q. Z. Yin, H. Y. Chen, J. H. Pan, Z. W. Zhang, Z. L. Zhuang, J. Y. Wan and W. D. Zhou, *Adv. Funct. Mater.*, 2025, **35**, 2422147.
- G. Feng, Q. Y. Ma, D. Luo, T. Z. Yang, Y. H. Nie, Z. Y. Zheng, L. X. Yang, S. B. Li, Q. Y. Li, M. L. Jin, X. Wang and Z. W. Chen, *Angew. Chem., Int. Ed.*, 2025, **64**, e202413306.
- Q. He, X. X. Liu, G. Xiao, X. H. He, W. B. Gong, L. F. Tang, Q. Chen, Q. C. Zhang and Y. G. Yao, *Small*, 2024, **20**, 2403660.
- T. Duan, J. M. Li, L. L. Li, Q. C. Sun, X. G. Lu and H. W. Cheng, *Energy Storage Mater.*, 2024, **73**, 103847.
- Z. Y. Zhang, S. Zhang, S. X. Geng, S. B. Zhou, Z. L. Hu and J. Y. Luo, *Energy Storage Mater.*, 2022, **51**, 19–28.
- C. X. Xian, S. Z. Zhang, P. Liu, L. Huang, X. P. He, S. H. Shen, F. Cao, X. Q. Liang, C. Wang, W. J. Wan, Y. Q. Zhang, X. Liu, Y. Zhong, Y. Xia, M. H. Chen, W. K. Zhang, X. H. Xia and J. P. Tu, *Small*, 2024, **20**, 2306381.
- Y. L. Liao, X. L. Wang, H. Yuan, Y. J. Li, C. M. Xu, S. Li, J. K. Hu, S. J. Yang, F. Deng, J. Liu and J. Q. Huang, *Adv. Mater.*, 2025, **37**, 2419782.
- Y. X. Wu, Z. Chen, K. Shi, Y. Wang, X. A. Li, Z. Q. Zhao, Q. Zhuang, J. Wang and M. H. Chen, *Energy Environ. Sci.*, 2025, **18**, 2817–2825.
- H. P. Liang, M. Zarrabeitia, Z. Chen, S. Jovanovic, S. Merz, J. Granwehr, S. Passerini and D. Bresser, *Adv. Energy Mater.*, 2022, **12**, 2200013.
- Y. X. Wu, Y. Li, Y. Wang, Q. Liu, Q. G. Chen and M. H. Chen, *J. Energy Chem.*, 2022, **64**, 62–84.
- W. Q. Fan, Y. Huang, M. Yu, K. H. She, J. R. Gou and Z. Zhang, *Nano Res.*, 2024, **17**, 2719–2727.
- N. Aspern, G. V. Rcschenthaler, M. Winter and I. C. Laskovic, *Angew. Chem., Int. Ed.*, 2019, **58**, 15978–16000.
- S. J. Xu, Z. H. Sun, C. G. Sun, F. Li, K. Chen, Z. H. Zhang, G. J. Hou, H. M. Cheng and F. Li, *Adv. Funct. Mater.*, 2020, **30**, 2007172.
- C. Z. Zhao, B. C. Zhao, C. Yan, X. Q. Zhang, J. Q. Huang, Y. F. Mo, X. X. Xu, H. Li and Q. Zhang, *Energy Storage Mater.*, 2020, **24**, 75–84.
- R. Y. Fang, B. Y. Xu, N. S. Grundish, Y. Xia, Y. T. Li, C. W. Lu, Y. J. Liu, N. Wu and J. B. Goodenough, *Angew. Chem., Int. Ed.*, 2021, **133**, 17842–17847.
- H. Nie, N. S. Schausser, J. L. Self, T. Tabassum, S. Oh, Z. S. Geng, D. Jones, M. S. Zayas, V. G. Reynolds, M. L. Chabinye, C. J. Hawker, S. Han, C. M. Bates, R. A. Segalman and J. R. Alaniz, *J. Am. Chem. Soc.*, 2021, **143**, 1562–1569.
- Z. G. Xue, D. He and X. L. Xie, *Mater. Chem.*, 2015, **3**, 19218–19253.
- H. Zhao, Z. Jia, W. Yuan, H. Hu, Y. Fu, G. L. Baker and G. Liu, *ACS Appl. Mater. Interfaces*, 2015, **7**, 19335–19341.
- Y. M. Zhao, L. B. Li, D. Zhou, Y. Ma, Y. H. Zhang, H. Yang, S. B. Fan, H. Tong, S. Li and W. H. Qu, *Angew. Chem., Int. Ed.*, 2024, **63**, e202404728.
- T. He, H. Cao and P. Chen, *Adv. Mater.*, 2019, **31**, 1902757.

- 39 L. Wang, J. W. Yan, R. Zhang, Y. F. Li, W. Z. Shen, J. L. Zhang, M. Zhong and S. W. Guo, *ACS Appl. Mater. Interfaces*, 2021, **13**, 9875–9884.
- 40 L. J. Liu, T. Wang, L. Sun, T. L. Song, H. Yan, C. L. Li, D. B. Mu, J. C. Zheng and Y. Dai, *Energy Environ. Mater.*, 2024, **7**, e12580.
- 41 Y. H. Li, Y. Y. Qin, J. Y. Zhao, M. B. Ma, M. Z. Zhang, P. Li, S. Y. Lu, H. T. Bu, K. Xi, Y. Q. Su and S. J. Ding, *ACS Appl. Mater. Interfaces*, 2022, **14**, 18360–18372.
- 42 Z. Y. Hu, Y. F. Zhang, Y. Zhang, J. Luo, W. J. Chen, W. Z. Fa, S. K. Huo, X. Jing, W. Bao, X. Y. Long and H. S. Cheng, *J. Power Sources*, 2022, **548**, 232052.
- 43 C. Fang, K. S. Huang, J. Zhao, S. Q. Tian, H. Dou and X. G. Zhang, *Nano Res.*, 2024, **17**, 5251–5260.
- 44 P. Didwal, Y. N. Singhababu, R. Verma, B. J. Sung, G. H. Lee, J. S. Lee, D. R. Chang and C. J. Park, *Energy Storage Mater.*, 2021, **37**, 476–490.
- 45 Y. L. Zhu, W. Li, L. Zhang, W. H. Fang, Q. Q. Ruan, J. Li, F. J. Zhang, H. T. Zhang, T. Quan and S. J. Zhang, *Energy Environ. Sci.*, 2023, **16**, 2825–2855.
- 46 Y. C. Liu, Z. K. Jin, Z. Y. Liu, H. Xu, F. R. Sun, X. Q. Zhang, T. Chen and C. Wang, *Angew. Chem., Int. Ed.*, 2024, **63**, e202405802.
- 47 T. Chen, B. Qin, Y. C. Liu, Z. K. Jin, H. P. Wu, C. Wang and X. Zhang, *CCS Chem.*, 2024, **6**, 1157–1164.
- 48 T. Chen, Y. C. Liu, Z. K. Jin, L. Sun, Z. Y. Liu, H. Xu, Z. G. Zhao and C. Wang, *Giant*, 2024, **19**, 100310.
- 49 Y. S. Li, X. D. Yang, Y. He, F. Li, K. F. yang, D. T. Ma, J. Feng, J. L. Huang, J. L. Zhao, M. Yang, Y. Y. Wang, Y. S. Xie, H. W. Mi and P. X. Zhang, *Adv. Funct. Mater.*, 2024, **34**, 2307736.
- 50 W. Lu, N. Wang, X. Liu, D. Chen, Q. Li, J. X. Rui, W. Q. Ning, X. Z. Shi, C. Li, Y. T. Zhao, A. He and Z. G. Teng, *J. Mater. Chem. B*, 2024, **12**, 7837.
- 51 S. Hao, L. Li, W. D. Cheng, Q. W. Ran, Y. Y. Ji, Y. X. Wu, J. S. Huo, Y. C. Yang and X. Q. Liu, *J. Mater. Chem. A*, 2022, **10**, 4881–4888.
- 52 N. Wu, P. H. Chien, Yu. M. Qian, Y. T. Li, H. H. Xu, N. S. Grundish, B. Y. Xu, H. B. Jin, Y. Y. Hu, G. H. Yu and J. B. Goodenough, *Angew. Chem., Int. Ed.*, 2020, **59**, 4131.
- 53 J. J. Zhang, J. F. Yang, T. T. Dong, M. Zhang, J. C. Chai, S. M. Dong, T. Y. Wu, X. H. Zhou and G. L. Cui, *Small*, 2018, **14**, 1800821.
- 54 A. Atik, D. Diddens, J. H. Thienenkamp, G. Brunklaus, M. Winter and E. Paillard, *Angew. Chem., Int. Ed.*, 2021, **60**, 11919.
- 55 L. B. Li and Y. H. Shan, *New Carbon Mater.*, 2021, **36**, 336–349.
- 56 Y. M. Zhao, L. B. Li, Y. H. Shan, D. Zhou, X. C. Chen, W. J. Cui and H. Wang, *Small*, 2023, **19**, 2301572.
- 57 F. Fu, W. Lu, Y. Zheng, K. Chen, C. Sun, L. N. Cong, Y. L. Liu, H. M. Xie and L. Q. Sun, *J. Power Sources*, 2021, **484**, 229186.
- 58 T. T. Lu, Y. J. Zhou, X. Y. Zeng, S. Hao and Q. Wei, *Mater. Lett.*, 2024, **360**, 135912.
- 59 F. Croce, G. B. Appetecchi, L. Persi and B. Scrosati, *Nature*, 1998, **394**, 456–458.
- 60 Z. Xu, T. Yang, X. Chu, H. Su, Z. X. Wang, N. J. Chen, B. N. Gu, H. P. Zhang, W. L. Deng, H. T. Zhang and W. Q. Yang, *ACS Appl. Mater. Interfaces*, 2020, **12**, 10341–10349.
- 61 X. F. Wang, C. K. Fu, Z. J. Feng, H. Huo, X. C. Yin, G. L. Gao, G. P. Yin, L. J. Ci, Y. J. Tong, Z. X. Jiang and J. J. Wang, *Chem. Eng. J.*, 2022, **428**, 131041.
- 62 W. Liu, C. Yi, L. Li, S. Liu, Q. Gui, D. Ba, Y. Li, D. Peng and J. Liu, *Angew. Chem., Int. Ed.*, 2021, **60**, 12931–12940.
- 63 C. Wang, H. R. Zhang, S. M. Dong, Z. L. Hu, R. X. Hu, Z. Y. Guo, T. Wang, G. L. Cui and L. Q. Chen, *Chem. Mater.*, 2020, **32**, 9167–9175.
- 64 F. P. Zhao, Q. Sun, C. Yu, S. M. Zhang, K. Adair, S. Z. Wang, Y. L. Liu, Y. Zhao, J. W. Liang, C. H. Wang, X. N. Li, X. Li, W. Xia, R. Y. Li, H. Huang, L. Zhang, S. Q. Zhao, S. G. Lu and X. L. Sun, *ACS Energy Lett.*, 2020, **5**, 1035–1043.
- 65 F. D. Han, A. S. Westover, J. Yue, X. L. Fan, F. Wang, M. F. Chi, D. N. Leonard, N. J. Dudney, H. Wang and C. S. Wang, *Nat. Energy*, 2019, **4**, 187–196.
- 66 D. C. Lin, P. Y. Yuen, Y. Y. Liu, W. Liu, N. Liu, R. H. Dauskardt and Y. Cui, *Adv. Mater.*, 2018, **30**, e1802661.
- 67 Y. X. Ma, J. Y. Wan, Y. F. Yang, Y. S. Ye, X. Xiao, D. T. Boyle, W. Burke, Z. J. Huang, H. Chen, Y. Cui, Z. Yu, S. T. Oyakhire and Y. Cui, *Adv. Energy Mater.*, 2022, **12**, 2103720.
- 68 Q. Zhou, J. Ma, S. M. Dong, X. F. Li and G. L. Cui, *Adv. Mater.*, 2019, **31**, e1902029.
- 69 Z. M. Guo, Y. P. Pang, S. X. Xia, F. Xu, J. H. Yang, L. X. Sun and S. Y. Zheng, *Adv. Sci.*, 2021, **8**, e2100899.
- 70 J. W. Tan, X. Ao, A. Dai, Y. F. Yuan, H. Zhuo, H. Lu, L. B. Zhuang, Y. X. Ke, C. L. Su, X. W. Peng, B. B. Tian and J. Lu, *Energy Storage Mater.*, 2020, **33**, 173–180.